SCA2003-41: A METHOD FOR ESTIMATING PERMEABILITY OF CARBONATE ROCKS FROM CT SCAN DATA

Ebrahim Hassanzadeh, S. Saleh Hendi, NIOC- Research Institute of Petroleum Industry;
Ayato Kato, JNOC- Technology Research Centre

This paper was prepared for presentation at the International Symposium of the Society of Core Analysts held in Pau, France, 21-24 September 2003

ABSTRACT

Permeability is one of the most important characteristics of hydrocarbon bearing formations. An accurate knowledge of permeability provides petroleum engineers with a tool for efficiently managing the production process of a field. Furthermore, it is one of the most important pieces of information in the design and management of enhanced recovery operations. Formation permeability is often measured in the laboratory from cores or evaluated from well test data.

CT scan data is widely used to calculate porosity and build 3D models of rock matrix in carbonates, but in this study we illustrate a method to use these data together with conventional laboratory measurements for estimating permeability of carbonate rocks. To do this core samples from a carbonate oil field in south west of Iran have been studied. The Permeability of samples was measured using a PDPK™ apparatus, the porosity of each sample was measured and CT slices were taken in constant intervals across the samples. Thin sections in the horizontal and vertical directions were prepared from the end pieces of the samples and were analyzed by using the optical microscope. For each core sample a column matrix containing average volumetric percentages of different minerals were assigned. CT numbers corresponding to each slice were exported in the form of a spreadsheet. All such spreadsheets that belong to the ith sample, together with porosity, column matrix and PDPK™ average permeability were called "i^{th} data set". All data sets were considered as training examples of a back propagation artificial neural network, whilst the target was permeability. Validation of the network results was achieved by leaving out some of the data sets and comparing their measured permeabilities with calculated ones. To decrease calculation time, up scaling was applied on CT data by scales of 2:1, 4:1, 8:1, 16:1 and 32:1 and results were compared with each other. A better understanding of the relationship between volume percentage of minerals, porosity, CT scan data and permeability of carbonates is developed from this study.

INTRODUCTION

Acquiring knowledge on formation permeability in carbonate reservoirs has remained one of the fundamental challenges to petroleum engineers. This important piece of information about porous rock provides engineers with the ability to design and manage efficient processes in the development of oil and gas fields. Using coring tools and bringing samples of the pay zone to the surface and measuring their permeability under

simulated downhole conditions is one of the oldest practices for estimating the formation permeability. Coring every well in a large field can be very expensive. It is necessary and inevitable to core some wells no matter how small or large a field. On the other hand, trying to get a representative sample from every single well, especially in fields with hundreds of wells, requires a large amount of capital. In a heterogeneous field where permeability values tend to change rapidly with spatial coordinates, such practices (coring every well), although expensive, would provide valuable information. Having a representative value for permeability in different locations, especially where wells (injection or production) are drilled could be used effectively in reservoir simulation studies.

Oil and oil service companies began using CT and MRI imaging technologies in the mid-1980s. The Oil industry uses X-ray Computerized Tomography (CT) and Magnetic Resonance Imaging (MRI) to characterize rock samples (cores) taken from wells. The industry is interested not only in topological issues concerning the structure of the rock samples or fluid boundaries; but, it is also essential to quantify the three-dimensional distribution of properties such as density and effective atomic number.

During the past several years, the number of successful applications of neural networks to solve complex problems has increased exponentially. Considerable attention has been devoted to the use of neural networks as an alternative approach to interpolation and extrapolation, pattern recognition, statistical, and mathematical modeling [1]. For example, back-propagation neural networks were used to develop process models as substitutes for complicated empirical and mathematical models [2]. These models can be used as an alternative to statistical and time series analysis. Neural network analysis, unlike regression, does not require specification of structural relationships between the input and output data. However, identification using neural networks is more useful when large amounts of data are available. Some CT data volumes may consist of 1000×1000×1000 pixels (or voxels) and artificial neural networks could significantly help geoscientists to identify relationships between different types of core properties and CT data.

PROCEDURES

Basics of X-ray CT Scanning

Computed X-ray tomography, or X-ray CT, is a completely non-destructive means of examining the interiors of opaque solid objects. It produces two-dimensional images (called "slices") that reveal the interior of an object as if it had been sliced open along the image plane for viewing. Contrast in an X-ray CT image is generated by differences in X-ray absorption that arise principally from differences in density within the object.

To produce tomographic images, X-rays pass through the object along several different paths in several different directions, resulting in an image that displays differences in density at each of several thousand points in a two-dimensional slice through the object tomography. The values attained when the detectors are read represent the beam

attenuation by an object placed in the path of the X-rays. The detectors are in a stationary array surrounding the object. The X-ray beams are always directed through the object aperture as the source moves around it in a circular path. The detectors are read at small rotational intervals and the resulting data are stored in a computer. This rotational excursion is called a pass and the total data acquired during this pass are termed a slice. After all readings for a slice have been acquired and stored in a computer, a cross-sectional image or matrix of attenuation coefficients μ(x, y) is created. Radon [3] established the mathematical foundation for image reconstruction from projection data. The basic synthetic unit is the volume element or voxel. The CT slice is composed of many voxels, each with its own characteristic attenuation, which are displayed as a 2-D image matrix of picture elements (pixels), shown in Figure1.

While this technique was originally developed for medical diagnosis, a similar technique has recently found industrial application. Industrial CT instruments are conceptually similar to those used for medical diagnosis, but are capable of significantly higher X-ray intensity and markedly higher spatial resolution. As a result, it is now possible to image the interiors of geological samples with remarkable clarity.

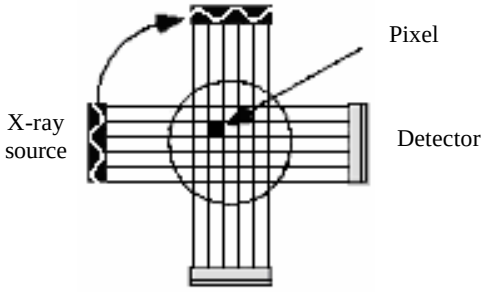

Figure 1. Schematic of CT scanning process.

The intensity data can be converted to an image representing differences in X-ray attenuation in the specimen by using Beer's law [4] to relate the incident intensity (*Io*) and the final intensity (*I*) to the object's linear attenuation coefficient (*μ)*:

$$I = I_0 \cdot exp\int_0^d [-m(x)]\,dx \qquad (1)$$

in which *d* is a distance coordinate along the X-ray path and *x* is a dummy variable of integration over distance. The unknowns in Equation (1) are the values of *μ(x)*, that is, the values of the linear attenuation coefficient at each point along each X-ray path. Differentiation of features within the object is possible because *μ* at each point depends directly on the density of the object at that point (?), on the effective atomic number of the material comprising the object at that point (*Z*) and the energy of the incoming X-ray beam (*E*) according to:

$$m = r \cdot (a + \frac{bZ^{3.8}}{E^{3.2}}) \qquad (2)$$

in which a is a quantity with a relatively small energy dependence, and b is a constant [5]. When a mixture of atomic species is present, Z (the effective atomic number) is defined by:

$$Z^{3.8} = \sum_i (f_i [Z_i]^{3.8}) \quad (3)$$

in which f_i is the fraction of the total number of electrons contributed by element i with atomic number Z_i.

Since it is impractical to deal with the X-ray attenuation coefficient, μ, a new scale is defined based on the international standard unit of Hounsfield (HU or CT number)[6]. On this scale, water has a value of zero and air has a value of -1000. Hence, each CT unit represents about a 0.1% change in the attenuation coefficient. Equation (4) defines the CT number:

$$CT = \frac{m_x - m_{water}}{m_{water}} \times 1000 \quad (4)$$

where μ_x is the calculated X-ray attenuation coefficient. In most CT scanners, the range of CT unit varies from -1000, representing air, to 4000, representing very dense materials. Reservoir rocks typically fall in the range of 1000 to 2000 on this scale (Table 1).

Table 1. Linear attenuation coefficients (μ) and CT numbers for some common mineral end-members. The tabulated values are calculated specifically for 120keV X-ray energy (modified from University of Texas's web site).

Mineral Name	Idealized Formula	Mass Density (g/cm^3)	μ (cm^{-1})	CT Number
Quartz	SiO_2	2.65	0.448	1275
Muscovite	$KAl_3Si_3O_{10}(OH)_2$	2.83	0.490	1323
Hedenbergite	$CaFeSi_2O_6$	3.63	0.823	2005
Calcite	$CaCO_3$	2.71	0.530	1384
Dolomite	$CaMg(CO_3)_2$	2.87	0.513	1357
Microcline	$KAlSi_3O_8$	2.56	0.452	1279
Rutile	TiO_2	4.25	0.955	2326
Diopside	$CaMgSi_2O_6$	3.23	0.601	1513
Albite	$NaAlSi_3O_8$	2.62	0.436	1266
Fayalite	Fe_2SiO_4	4.39	1.22	2993
Magnetite	Fe_3O_4	5.22	1.62	4000

Sample Description

This study is carried out on 34 core samples that have been taken from Sarvak Formation in four exploration wells located in the south west of Iran. The limestones of the overlying Sarvak Formation (Albian – Turonian) formed during the high stand. A major sea-level fall at the Cenomanian – Turonian boundary exposed carbonates of the Sarvak Formation. However, the uppermost portion of the Sarvak Formation was deposited

during an early Turonian sea-level rise, and was subsequently exposed due to a minor sea-level fall. Major diagenetic alterations occurred along the Cenomanian - Turonian unconformity. Meteoric processes resulted in karstification, generation of porosity and permeability, and dolomitization, forming good reservoir quality strata in the Sarvak Formation. Burial diagenesis affected all units, in some cases increasing porosity and permeability and in others decreasing them [7]. Investigating correlations between permeability and other petrophysical properties in carbonate rocks is not as straightforward as in sandstones. For example different types of porosity in carbonate rocks such as vugs, micro-fractures, intragranular and intergranular porosity, results in permeability variations for the same porosity. Therefore considering other types of available data to estimate permeability in carbonates could increase accuracy of the results.

The depth of sampling was determined based on petrophysical and geological logs in the four exploration wells. The samples were prepared as cylindrical shape plugs; these samples are plugged vertically and are 1.5" in diameter and 2.5" in length (Figure 2-a). After preparation of samples, precise physical measurements were taken, (including mass, diameter and length) and then the porosity and permeability of samples were determined. Densities were achieved by calculating mass/volume ratios for each sample, porosities were determined using an ASC300 porosity meter and permeability measured by a pressure decay profile permeametry (PDPK™) apparatus. To measure permeability of samples they were located in the specific place of apparatus and pressure decays were measured in two orthogonal directions (as shown in Figure 2-a) in 1cm constant intervals along the sample's main axis. Average of all measured values for each core sample is called "Average Horizontal PDPK™ Permeability" of the sample.

Scanning Procedure

An Xforce Toshiba CT scanner (third generation) at JNOC- Technology Research Centre was used in this study. The scanner consists of a mainframe, rotational elements, and scanner electronics. The mainframe houses the X-ray source, detector array, and beam shaping elements. The scanner assembly consists of a support table for positioning the core. The generator group is responsible for generating the X-rays. The control panel consists of a video console, an interactive keyboard for viewing, initiating image generation, and for image manipulation. The computation unit performs sequencing, interprets instructions, and executes them. The Image Processing System accepts image information in digital form and converts it to the image seen on the viewing monitors. Processed images including digital data have been stored in appropriate storage media such as magnetic disks.

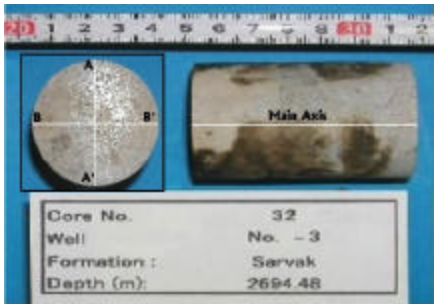

Figure 2-a. Sample photo-montage of core plugs.

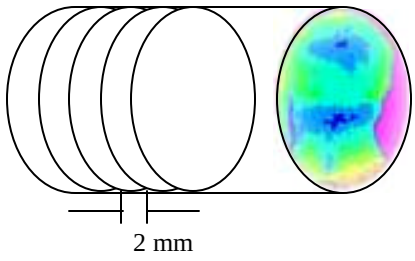

Figure 2-b. Schematic of the CT slices along the sample.

Figure 3 displays the scanner components. The cores were initially cleaned, dried and then scanned at room pressure and temperature at an energy level of 120 keV and a field size of 18 cm. A small field of scan was used to obtain better spatial resolution, as the number of pixels available remains constant. Slices were taken in 2 mm constant intervals along each sample as it is displayed in Figure 2-b.

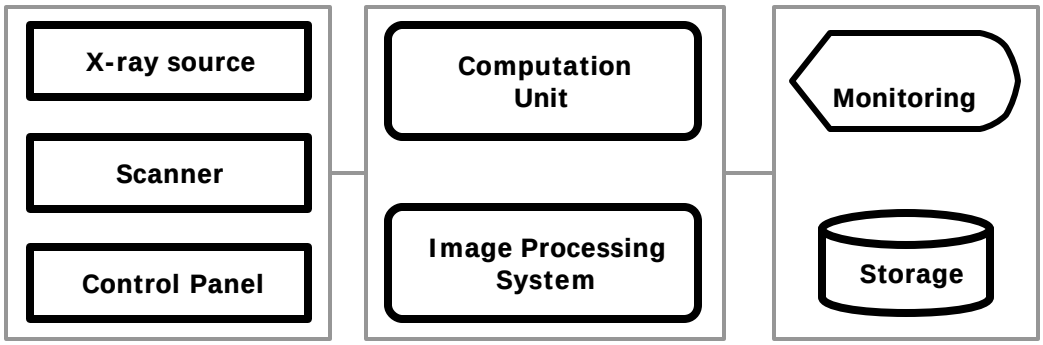

Figure 3. The scanner system.

Slice thickness was made as small as possible, ie., 1 mm (it varies from 1-10 mm), in order to minimize errors and maximize resolution. Greater slice thickness results in greater measurement error. The size for each CT slice is 112 3 112, and each pixel represents a volume of 0.35 mm 3 0.35 mm 3 1 mm. The average CT value within each pixel has been considered as CT value of the pixel. Figure 4 shows a series of CT images obtained for each core sample.

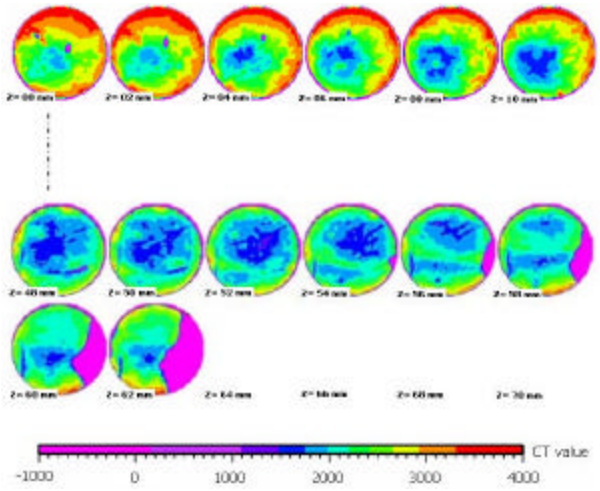

Figure 4. A series of CT images obtained for core samples.

Data Set Arrangement

CT data of a core sample consists of 32 matrices each of 112 3 112 size which in mathematical notation can be showed as CT(i,j) & i,j= 1,2,…,112. To reduce size of CT

data and consequently calculation time, the average of each CT slice has been considered as representative of that slice. In this study we considered 6 data sets of different scales for each sample. First set consists of 32 CT slice averages together with porosity, depth of samples, bulk density and volume percentage of minerals as input , and permeability of samples as output part of data. The second, third, forth and fifth data sets consist of all information of first data set, but the difference is in scale of CT data. The number of CT averages has been reduced by scales of 1/2, 1/4, 1/8 , 1/16 and 1/32 as shown in figure 5.

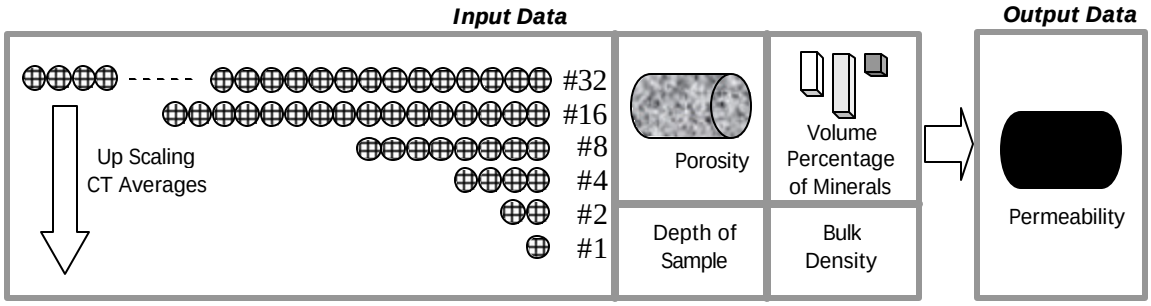

Figure 5. Schematic of data sets .

Up scaling the CT averages is done using a simple averaging method:

$$
\begin{aligned}
k = 1,2,\ldots,112 \;\; i, j = 1,2,\ldots,32 \text{ (Slice No.) } \& \quad & A_k^{[32]} = \Big(\sum_{i,j} CT(i,j)\Big)/12544 \\
l = 1,2,\ldots,16 \quad & A_l^{[16]} = (A_{2l}^{[32]} + A_{2l-1}^{[32]})/2 \\
l = 1,2,\ldots,8 \quad & A_l^{[8]} = (A_{2l}^{[16]} + A_{2l-1}^{[16]})/2 \\
l = 1,2,3,4 \quad & A_l^{[4]} = (A_{2l}^{[8]} + A_{2l-1}^{[8]})/2 \\
l = 1,2 \quad & A_l^{[2]} = (A_{2l}^{[4]} + A_{2l-1}^{[4]})/2 \\
& A^{[1]} = (A_1^{[2]} + A_2^{[2]})/2
\end{aligned}
\qquad (5)
$$

NETWORK STRUCTURE DESIGN

Known as sixth generation computing, neural networks are widely used in many disciplines from weather forecast to airport security devices. Neural networks are analog, distributive and parallel information processing methods that have proven to be powerful pattern recognition tools [8]. Since they process data and learn in a parallel and distributed fashion, they are able to discover highly complex relationships between several variables that are presented to the network. As a model-free function estimator, neural networks can map input to output no matter how complex the relationship. There are several paradigms that can be used to generate neural networks. To achieve the goal of this study, a feed forward, back propagation neural network (which adopts a supervised training scheme) has been used. An artificial neural network is a system of several simple processing units known as nodes, neurons or processing elements. These processing elements are associated with one another through simple connections known

as synaptic connections. The strength of the synaptic connections changes with attaching a weight to them. Figure 6 is a schematic diagram of a typical artificial neural network.

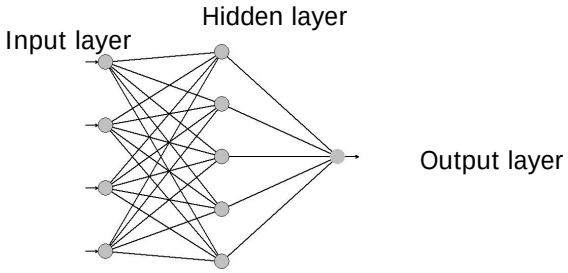

Figure 6. Schematic of an Artificial Neural Network.

Neurons in a network are organized in layers. Each layer is responsible for a particular task. Typically there are three kinds of layers in an artificial neural network. Input layer is responsible for presenting the network with the necessary information from the outside world in a normalized manner. Hidden layers (there may be more than one hidden layer in a network, this is a problem dependent factor) contain hidden neurons that are responsible for the main part of the input to output mapping. These neurons are responsible for feature extraction from the input neurons and subsequently passing the information to the output neurons. Output layer contains output neurons that communicate the outcome of the neural networks computation with the user. The back-propagation learning rule that is used in this study, is introduced below [9]:

output state of j^{th} node in layer s $X_j^{[s]}$

connection weight joining i^{th} node in layer (s-1) to j^{th} node in layer s $W_{ji}^{[s]}$

weighted summation of inputs to j^{th} node in layer s $I_j^{[s]}$

A processing element of a feed-forward network transfers its inputs as follows:

$$X_j^{[s]} = f\left(\sum_i \left(W_{ji}^{[s]} \cdot X_j^{[s-1]}\right)\right) = f\left(I_j^{[s]}\right) \quad (6)$$

where f is a transfer function. The function f can be any smooth function for a processing element. The sigmoid function is used as the transfer function in this study. After selecting neural network structure, samples for training and testing the network are collected as described in Figure 5. During the supervised training, it was necessary to provide the network with the correct permeability value for each example. The network will converge to the correct permeability value by back propagating the error between its prediction and the actual permeability value.

RESULTS

Figure 7 shows the relationship between sample permeability and CT average, depth, percentages of calcite, and dolomite, respectively. The scatter of these plots and low

correlation coefficients (except for CT average that is a function of density) suggest no apparent relationship between these parameters and formation permeability.

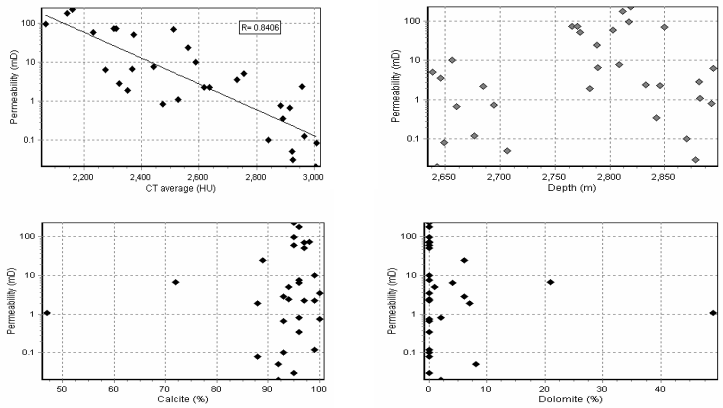

Figure 7. Relationships between permeability with other data of samples.

Samples were divided into two sets, one set containing 22 samples for analysis or learning and another set of 12 samples for testing of the results. We performed multiple linear regression on the analysis data set to achieve a general formula for calculating permeability using other available parameters of the samples as shown in Figure 8-a. The correlation coefficient is moderate. Figure 8-b is a comparison between the actual permeability of samples and calculated values. The correlation coefficient is good.

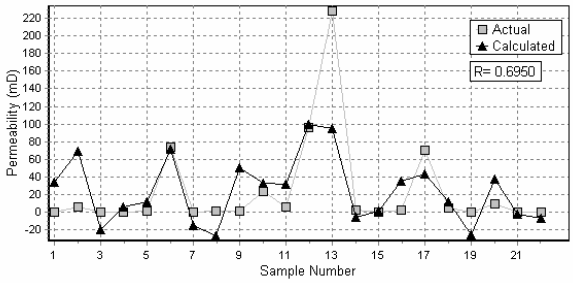

Figure 8-a. Comparison between measured with calculated permeability values of 22 core samples obtained from multiple linear regression.

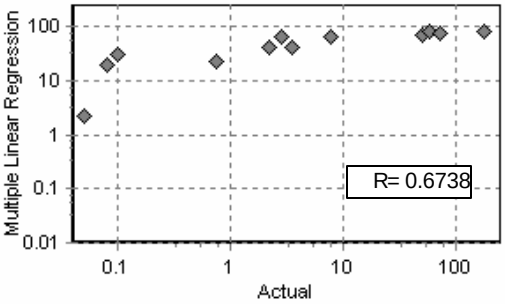

Figure 8-b. Cross plot of measured and calculated permeability values of 12 test samples obtained from multiple linear regression.

The networks were trained and then tested to see if they were able to estimate/predict permeability values from the four wells in Sarvak formation. The 12 samples that were chosen randomly in this study for test purposes (and were never seen by networks during the training) included a wide range of permeabilities from 0.05 to 179.15 mD. This further indicates the high degree of heterogeneity of this formation. Figure 9 shows the actual permeability values of test samples that were measured in the laboratory in comparison with the network's estimation/prediction for each sample. Although permeability values cover a wide range, the network is able to follow the trend very closely. This figure show's an increase in accuracy of predictions as the number of CT

averages (NN CT [#]) is increased, specially for the samples with low permeability. After plotting core measurements versus network predictions, one can see the divergence of the predictions from a perfect match, which is the unit slope line.

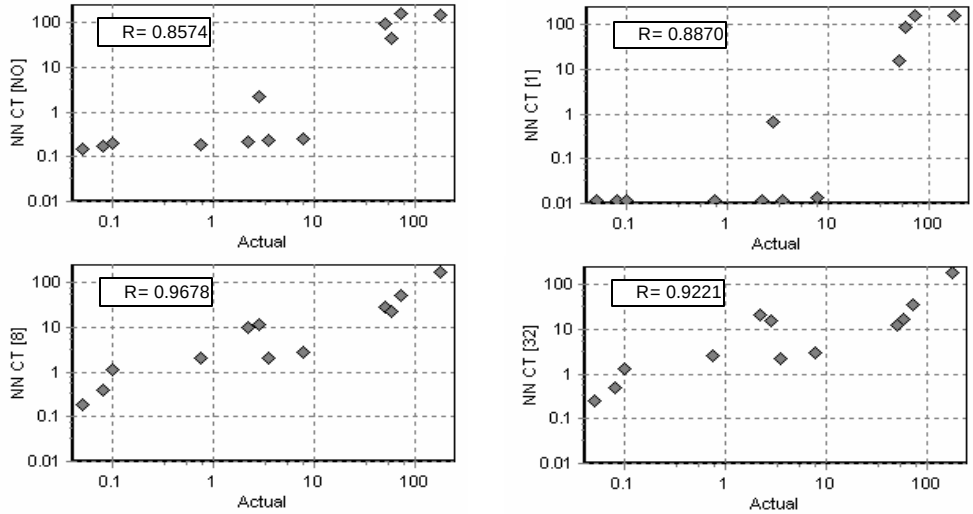

Figure 9. Comparison between results of ANNs containing different numbers of CT averages.

Figure 10 displays effect of up scaling the CT averages on permeability prediction. Comparing the results presented in Figures 9 and 10 with that of Figures 8 and 7 reveals the power of artificial neural networks in pattern recognition. One might comment on the input variables that were used in this study in the following fashion: CT numbers are related to the density, topology and structure of medium and consequently are related to the fractures that have doubtless influence on permeability. Depth of the formation is an indication of reservoir pressure that might affect permeability. Percentage of minerals cause changes in wettability which has a direct impact on permeability.

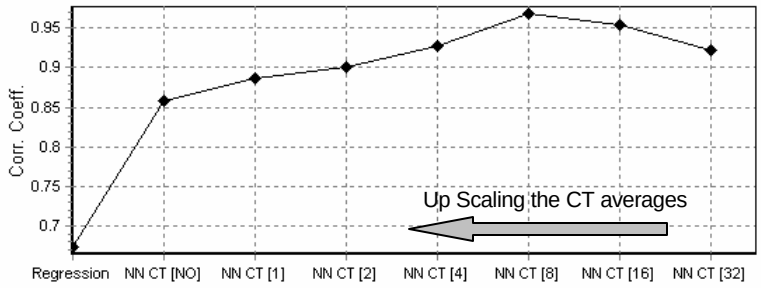

Figure 10. Effect of Up Scaling on Permeability prediction.

DISCUSSION

The results presented here are based on data of 34 samples taken from four wells. A few points about these results need to be mentioned. Our experience with the design and development of neural networks for permeability prediction/estimation has shown that it is essential to have enough data to train the network properly in order to see acceptable, as well as repeatable, results. The questions of how much data is enough and whether

there exists a threshold below which neural nets will not be effective are currently under investigation. The results are as good as the data available. With proper data more can be done with neural networks than any other tool.

CONCLUSIONS

This study showed that neural network estimation of carbonates permeability using CT scan data is a feasible methodology. Artificial neural networks that are capable of predicting/estimating carbonate permeability using CT scan and laboratory data were presented. It was shown that the trained networks were able to predict/estimate permeability comparable to that of actual core measurements. Availability of reliable core data for training process proved to be essential. At this point, this type of study is capable of producing lab specific results. Adequate knowledge on fundamental theories and practices of artificial neural networks are required to achieve acceptable and repeatable results. Treating neural nets as black boxes may prove to be disappointing.

ACKNOWLEDGEMENT

The authors would like to thank JNOC- Technology Research Centre and NIOC-Research Institute of Petroleum Industry for their laboratory resources, data release and permission to publish this paper.

NOMENCLATURE

a	= Klein-Nishira coefficient
b	= constant in Eq. (2), 9.8(10-24 ,mL2/t2, keV3.2
E	= energy level, mL2/t2, keV
I	= detected X-ray intensity, 1/t, counts/min
I0	= incident X-ray intensity, 1/t, counts/min
? ?	≑ density, m/L3, gm/cc
μ	= linear attenuation coefficient, L^{-1}, cm^{-1}
x	= thickness of material, L, mm
Z	= atomic number
CT	= CT number
HU	= Hounsfield unit
R	= linear correlation coefficient

NN CT[i] = set of neural net predictions using i number of CT averages

REFERENCES

[1] Murray, A. F., *Applications of Neural Networks*, Kluwer Academic Publishers, Boston, (1995), pp. 129-150.

[2] Nikravesh, M., *Dynamic Neural Network Control*, Ph.D. Dissertation, University of South Carolina, Columbia, SC, (1994).

[3] Radon, J., " Uber die Bestimmung von Funktionen durch ihre Integralwerte langs gewisser Mannigfaltigkeiten", *Ber. Verb. Saechs. Akad. Wiss., Math. Phys. KI.*, (1917) **69**, pp. 262-277.

[4] Herman, G. T., *An Introduction to Some Basic Mathematical Concepts of Computed Tomography*, Roentgen-Video-Techniques for Dynamic Studies, Ed. P. heintzen and J. Bursch, Georg Thieme Publishers, Stuttgart, Germany, (1978), pp. 253-260.

[5] Wellington, S. L., Vinegar, H. J., "X-ray Computerized Tomography", *Journal of Petroleum Technology*, (1987) **8**, pp. 885-898.

[6] Hounsfield, G. N., *A Method of an Apparatus for Examination of a Body by Radiation Such as X-ray or Gamma Radiation*, U.K. Patent No.1283915, (1972).

[7] Kayvani, F., Heydari, E, "Depositional environments and diagenesis of cretaceous (albian to maasterichtian) strata of the Abadan plain of the Persian platform in southwestern of Iran", *Proceedings of The Geological Society of America Annual Meeting, Denver, CO*, (2002).

[8] Fausett, L., *Fundamentals of Neural Networks*, Prentice-Hall, USA, (1994), pp. 289-330.

[9] Bishop, M.C., Bishop, C., *Neural Networks for Pattern Recognition*, Oxford University Press, USA, (1996), pp. 116-160.